Electronic Supplementary Information on

Synthesis of a two-dimensional organic-inorganic bismuth iodide metalate through *in situ* formation of iminium cations

Natalie Dehnhardt, Jan-Niclas Luy, Marvin Szabo, Mirco Wende, Ralf Tonner and Johanna Heine**

Department of Chemistry and Material Sciences Center, Philipps-Universität Marburg, Hans-Meerwein-Straße, 35043 Marburg, Germany.

*E-mail: tonner@chemie.uni-marburg.de

johanna.heine@chemie.uni-marburg.de

Synthetic Details

General. BiI_3 was synthesized from the elements according to literature procedures.[1] Dimethylamine (40 % solution in water) and HI (57 % solution in water, stabilizer: 0.75 % H_3PO_2) were used as supplied from commercial sources. Pentane, ethanol and pyridine were flash-distilled prior to use. Acetone was dried by standing over activated 3 Å molecular sieve. $(Me_2NH_2)I$ was prepared from aqueous solutions of dimethylamine and HI. The reference compound $(Hpy)BiI_4$ (HPy^+ = pyridinium, $C_5H_5NH^+$) was prepared by mixing stoichiometric ratios of BiI_3 and (HPy)I (prepared from pyridine and HI solution) in ethanol for 24 hours at room temperature.[2] A single crystal of $(Hpy)BiI_4$ was identified from its SCXRD cell parameters at 100 K. We note that there is likely a phase transition between 100 K and room temperature, as the PXRD pattern of the crushed single crystal recorded at room temperature did not completely match the simulation. CHN analysis was carried out on an Elementar CHN-analyzer. Details on additional analysis methods can be found in the respective sections below.

$(Me_2C{=}NMe_2)Bi_2I_7$ (1). Under inert conditions, BiI_3 (119 mg, 0.2 mmol) and $(Me_2NH_2)I$ (18 mg, 0.1 mmol) were suspended in 5 mL dry acetone and heated to reflux for 1.5 hours. While cooling down to room temperature, the solid product precipitated. It was washed with pentane and dried under vacuum. $(Me_2C{=}NMe_2)Bi_2I_7$ (**1**) was obtained as dark red microcrystalline powder.

(Yield: 86.7 mg, 0.062 mmol, 62 %). Data for **1**: Anal. Calcd for $C_5H_{12}Bi_2I_7N$, (M = 1392.39 g mol^{-1}): C, 4.31; H, 0.87; N, 1.01 %. Found: C, 4.66; H, 0.87; N, 1.07 %.

Single crystals of **1** were grown by suspending BiI_3 (119 mg, 0.2 mmol) and Me_2NH_2I (18 mg, 0.1 mmol) in 10 mL of dried acetone under inert conditions. The suspension was heated to reflux for 1.5 hours, transferred to a second Schlenk tube and cooled down slowly. Very small dark red crystals of **1** were obtained after 24 hours.

Crystallographic Details

Table S1: Crystallographic data for **1**.

	1
Empirical formula	$C_5H_{12}Bi_2I_7N$
Formula weight /g·mol^{-1}	1392.42
Crystal color and shape	dark red block
Crystal size	0.078 × 0.049 × 0.04
Crystal system	monoclinic
Space group	*P*2/*n*
a /Å	14.4647(8)
b /Å	7.5084(4)
c /Å	20.9965(11)
α /°	90
β /°	108.165(2)
γ /°	90
V /Å^3	2166.7(2)
Z	4
ρ_{calc} /g·cm^{-3}	4.269
μ(Mo$_{K\alpha}$) /mm^{-1}	26.177
measurement temp. /K	100
Absorption correction type	multi-scan
Min/max transmission	0.2865/0.3311
2Θ range /°	5.426-50.644
No. of measured reflections	83909
No. of independent reflections	3936
R(int)	0.0623
No. of indep. reflections ($I > 2\sigma(I)$)	3402
No. of parameters	142
R_1 ($I > 2\sigma(I)$)	0.0222
wR_2 (all data)	0.0367
S (all data)	1.111
$\Delta\rho_{max}$, $\Delta\rho_{min}$ /e· Å^{-3}	0.91/-1.26

Details of crystal structure measurement and refinement: Single crystal X-ray determination was performed at 100 K on a Bruker Quest D8 diffractometer with microfocus MoKα radiation and a Photon 100 (CMOS) detector. The structure was solved using direct methods, refined by full-matrix least-squares techniques and expanded using Fourier techniques, using the ShelX software package[3] within the OLEX2 suite.[4] All non-hydrogen atoms were refined anisotropically. Hydrogen atoms were assigned to idealized geometric positions and included in structure factors calculations. Pictures of the crystal structures were created using DIAMOND.[5] Data was deposited as CCDC 1939881.

The carbon and nitrogen atoms in the iminium cation's central C=N bond were found to be occupationally disordered and modelled accordingly. C/N occupancies were refined with a common free variable, allowing preferred occupancies (C=N vs. N=C) to manifest, but keeping the overall model chemically sensible. Nonetheless, occupancies refined close to 0.5. In line with common practice for modelling occupational disorder, EXYZ and EADP constraints were used on both positions.

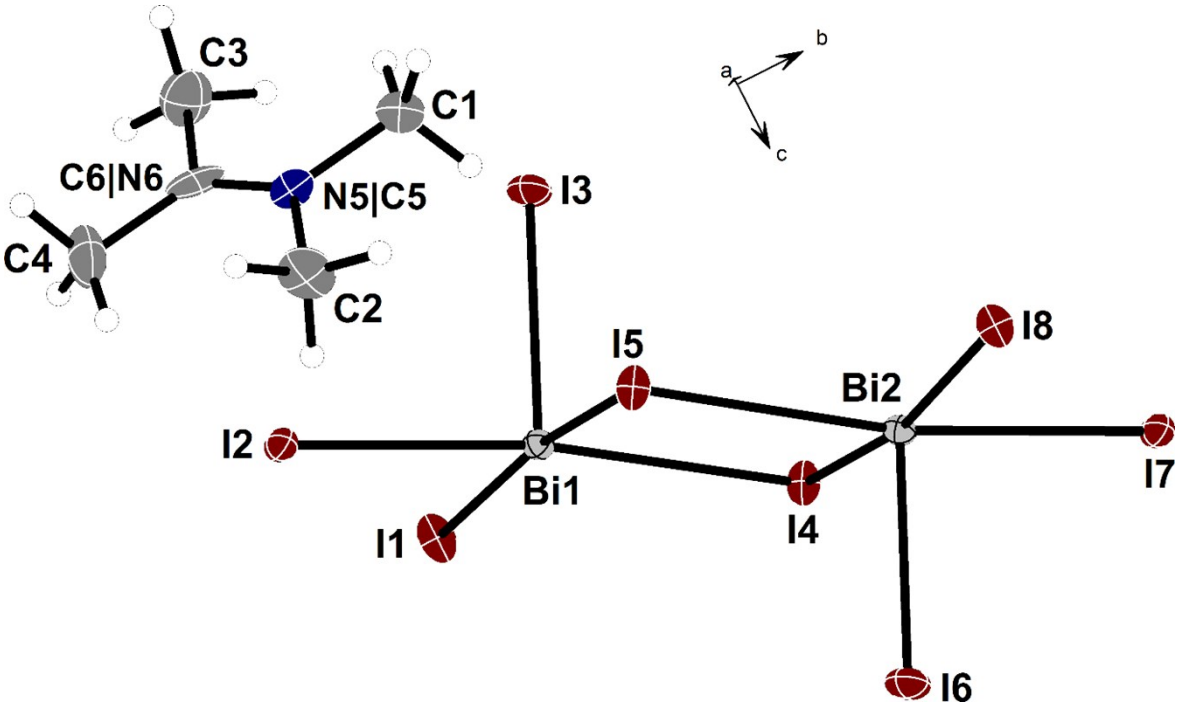

Figure S1: Asymmetric unit of **1**, ellipsoids at 70% probability, majority (0.53) position of disordered atoms in the C=N bond shown.

Table S2: Selected interatomic distances (in Å) and angles (in °) in **1**.

Symmetry operation: I +X,1+Y,+Z, II +X,-1+Y,+Z, III 1/2-X,+Y,3/2-Z, IV 3/2-X,+Y,3/2-Z

Bi2 I8	3.0966(3)	I8 Bi2 $I2^{I}$	83.846(9)	I5 Bi1 I1	171.991(11)
Bi2 I4	3.0626(5)	I8 Bi2 I5	88.478(12)	I5 Bi1 $I7^{II}$	85.957(11)
Bi2 $I2^{I}$	3.3375(4)	I4 Bi2 I8	169.250(11)	I1 Bi1 I4	89.578(12)
Bi2 I5	3.1577(4)	I4 Bi2 $I2^{I}$	85.409(11)	I1 Bi1 $I7^{II}$	86.160(10)
Bi2 I7	2.9875(4)	I4 Bi2 I5	90.971(11)	I3 Bi1 I4	94.928(12)
Bi2 I6	2.8907(4)	I5 Bi2 $I2^{I}$	85.318(11)	I3 Bi1 I2	92.237(12)
Bi1 I4	3.1522(4)	I7 Bi2 I8	86.535(12)	I3 Bi1 I5	91.383(12)
Bi1 I2	2.9896(4)	I7 Bi2 I4	92.634(12)	I3 Bi1 I1	96.476(11)
Bi1 I5	3.0512(5)	I7 Bi2 $I2^{I}$	87.250(11)	I3 Bi1 $I7^{II}$	77.186(13)
Bi1 I1	3.1001(4)	I7 Bi2 I5	171.454(12)	$Bi2^{III}$ I8 Bi2	125.283(18)
Bi1 $I7^{II}$	3.3513(4)	I6 Bi2 I8	97.917(11)	Bi2 I4 Bi1	88.816(12)
Bi1 I3	2.8885(4)	I6 Bi2 I4	92.825(12)	Bi1 I2 $Bi2^{II}$	93.009(11)
I8 $Bi2^{III}$	3.0966(3)	I6 Bi2 $I2^{I}$	178.182(13)	Bi1 I5 Bi2	88.916(12)
I2 $Bi2^{II}$	3.3377(4)	I6 Bi2 I5	95.157(13)	Bi1 I1 $Bi1^{IV}$	125.151(19)
I1 $Bi1^{IV}$	3.1001(3)	I6 Bi2 I7	92.402(12)	Bi2 I7 $Bi1^{I}$	92.773(11)
I7 $Bi1^{I}$	3.3513(4)	I4 Bi1 $I7^{II}$	86.057(11)	C6 N5 C1	122.2(5)
N5 C6	1.283(7)	I2 Bi1 I4	171.855(12)	C6 N5 C2	122.8(5)
N5 C1	1.489(8)	I2 Bi1 I5	92.408(12)	C2 N5 C1	114.9(5)
N5 C2	1.486(8)	I2 Bi1 I1	85.764(12)	N5 C6 C4	123.0(6)
C6 C4	1.481(8)	I2 Bi1 $I7^{II}$	86.966(11)	N5 C6 C3	121.3(5)
C6 C3	1.510(8)	I5 Bi1 I4	91.288(11)	C4 C6 C3	115.7(5)

Table S3: Comparison of bond length in Angstroms in the cation of **1** with literature references

	1	**$(Me_2C=NMe_2)ClO_4$[a]**	**$(Me_2C=NMe_2)BPh_4$[a]**
C=N	1.283(7)	1.30	1.291(8)
C-C, C-N	1.481(8)-1.510(8)	1.51	1.505(7)-1.515(7)

[a] Bond length according to [6] and [7], measured at room temperature. In both cases the cation is disordered about a mirror plane.

Table S4: Comparison of bond length in Angstroms in the anion of **1** with literature references

	1	**$(NMe_2H_2)_3[BiI_6]$[a]**	**$(dmes)_2[BiI_5]$**	**$(dim)_2[Bi_2I_{10}]$[c]**
$Bi\text{-}I_{terminal}$	2.8885(4) - 2.8907(4)	3.0342(8)- 3.0881(8)	2.9484(7)- 3.0775(6)	2.9821(6)- 3.1176(6)
$Bi\text{-}I_{corner\text{-}sharing}$	3.0966(3) - 3.1001(4)	-	3.2078(7)- 3.2405(7)	-
$Bi\text{-}I_{edge\text{-}sharing}$	2.9875(4) - 3.3513(4)	-	-	3.1757(5)- 3.2574(5)

[a] Bond length according to [8], measured at room temperature.

[b] dmes = dimethyl(2-ethylammonium)sulfonium; bond length in the corner-sharing zig-zag-chain according to [9], measured at room temperature.

[c] dim = diimidazolium $(C_9H_{14}N_4)^{2+}$; bond length in the edge-sharing dinuclear unit according to [10], measured at room temperature.

A fairly broad range of $Bi\text{-}I_{edge\text{-}sharing}$ bond length is observed in **1**, in line with the well-documented trans-effect in halogenido pentelates, e.g. $Bi\text{-}I_{edge\text{-}sharing}$ bonds trans to $Bi\text{-}I_{terminal}$ bonds are significantly longer than those trans to other $Bi\text{-}I_{edge\text{-}sharing}$ bonds. [11]

Thermal analysis

The thermal behavior of **1** (17.4 mg), was studied by TGA/DSC on a NETSCH STA 409 C/CD from 25 °C to 1000 °C with a heating rate of 10 °C min^{-1} in a constant flow of 100 ml min^{-1} N_2. A mass loss of 98.4 % starts at 290 °C. The DSC shows an endothermic peak at 258 °C. During visual inspection of a sample during heating, no melting of the sample at this temperature was observed, indicating a solid-solid phase transition.

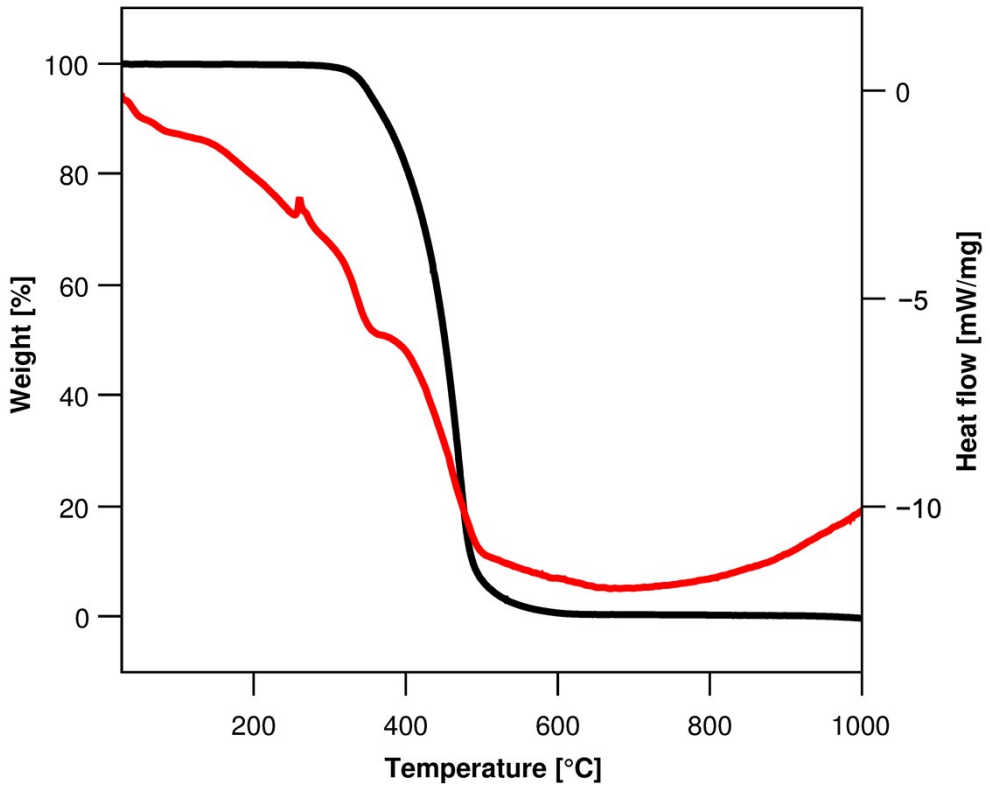

Figure S2. TGA and DSC of **1**.

Powder diffraction

Powder patterns were recorded on a *STADI MP* (*STOE* Darmstadt) powder diffractometer, with $CuK_{\alpha1}$ radiation with λ= 1.54056 Å at room temperature in transmission mode from 3 to 80° in 2θ. The pattern of **1** confirms the presence of the phase determined by SCXRD measurement and the absence of any major crystalline by-products. A study of the hydrolysis sensitivity of **1** was performed by first measuring a freshly prepared powder sample, followed by measuring a sample that was exposed to humidity. To provide a well-defined water-saturated atmosphere a Schlenk tube filled was filled with 10 mL of water. A sample of **1** was suspended above the surface of the water on a piece of scotch tape. The closed tube was kept at room temperature and the sample was removed and measured after 24 h. The pattern shows that **1** remains stable under these high humidity conditions. A study of the long term stability was also conducted, aging a sample in air for 5 months. The corresponding powder pattern shows that no significant decomposition takes place during this timeframe.

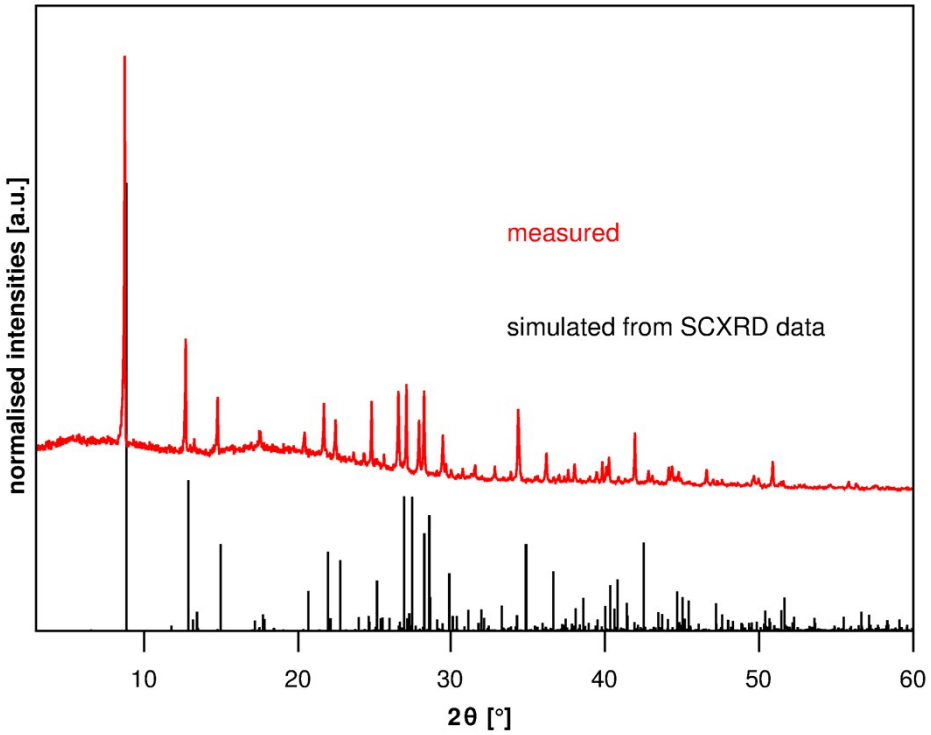

Figure S3. Powder diffraction pattern of **1**.

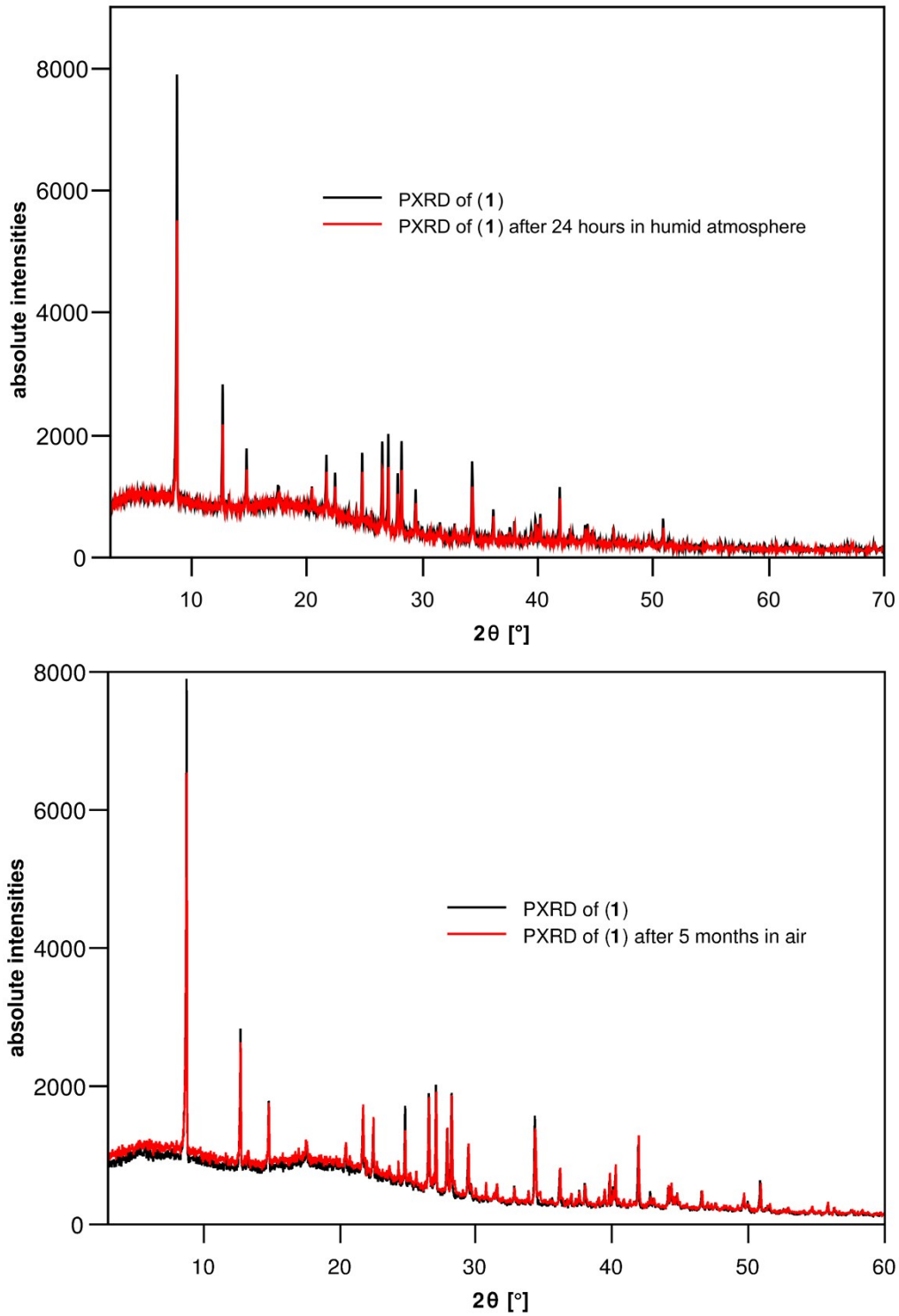

Figure S4. Powder diffraction patterns of a fresh sample of **1** in comparison with a sample stored in a water saturated atmosphere for 24h (top) and aged in air for 5 months (bottom). Data is not normalized or background-corrected to show that no increase in amorphous background below 30° in 2θ is observed between the two compared measurements. The difference in absolute intensities can likely be attributed to small differences in sample preparation such as the exact amount of substance or placement on the scotch tape and sample holder.

IR spectroscopy

An IR spectrum of **1** was recorded on a *Bruker Tensor 37* FT-IR spectrometer equipped with an ATR-Platinum measuring unit. The sample showed significant overall absorption in the measurement range. The characteristic band of the C=N group can be observed at 1666 cm^{-1}, close to values reported for $(Me_2N{=}CMe_2)Ag_2I_3$ (1680 cm^{-1})[12] and $(Me_2N{=}CMe_2)ClO_4$ (1687 cm^{-1}).[13]

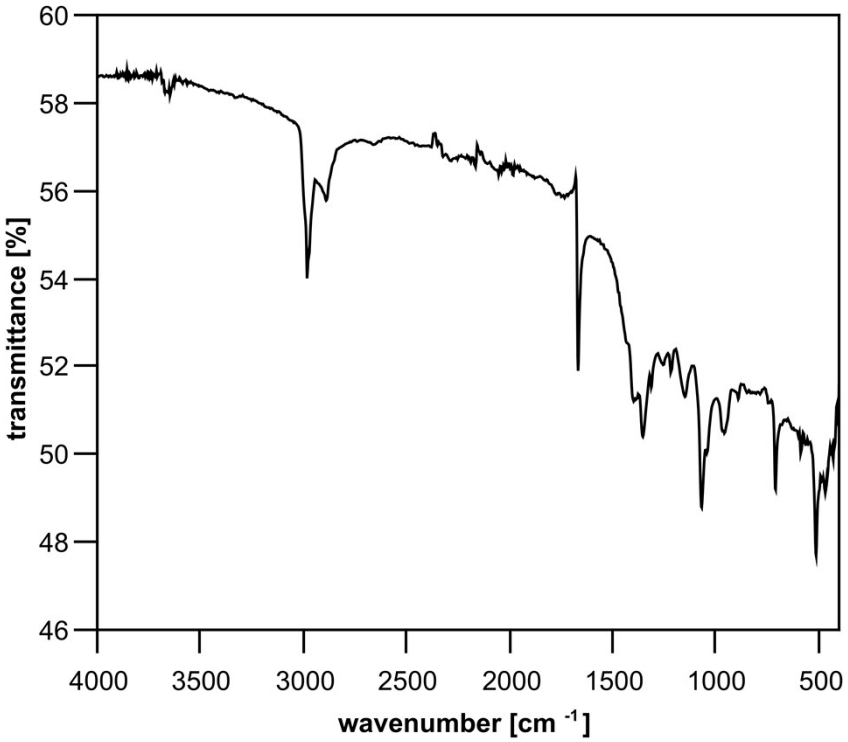

Figure S5. IR spectrum of **1**.

Raman Spectroscopy

A Raman spectrum of **1** was recorded on a confocal Raman microscope (*Monovista CRS+, S&I*) with 633 nm laser excitation. Strong bands are observed at 140, 110 and 65 cm^{-1}, which can be tentatively assigned to Bi-$I_{terminal}$ and Bi-$I_{bridging}$ stretching modes[14] and I-Bi-I scissoring modes,[15] respectively.

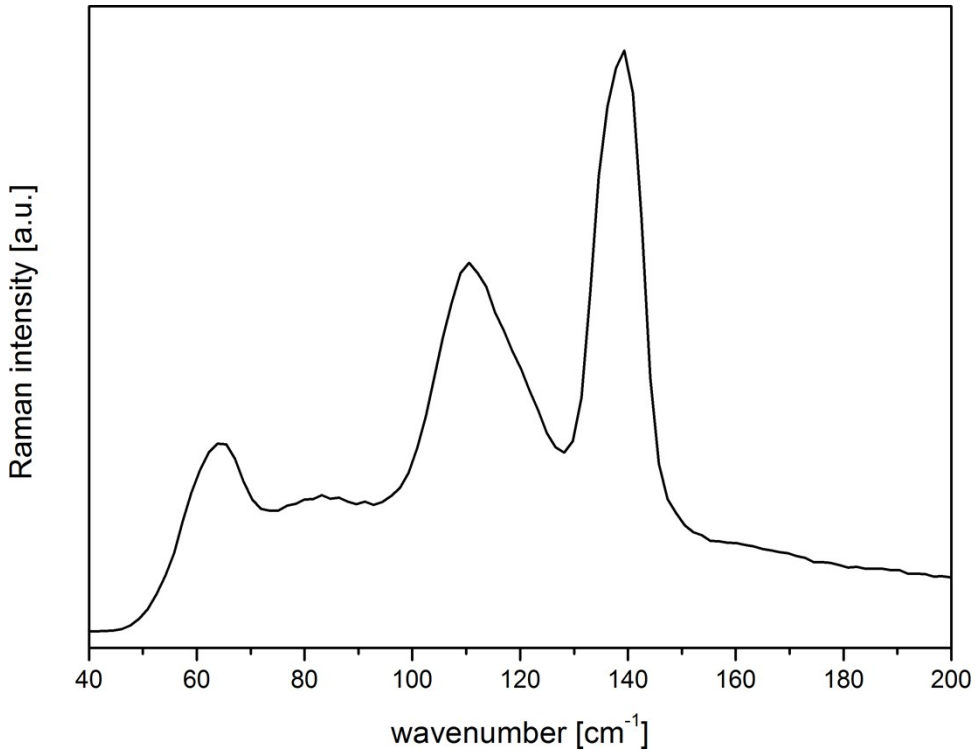

Figure S6. Raman spectrum of **1**.

Optical properties

Optical absorption spectra were recorded on a *Varian Cary 5000* UV/Vis/NIR spectrometer in the range of 200-800 nm in diffuse reflectance mode employing a Praying Mantis accessory (*Harrick*). An onset of absorption can be observed at 671.5 nm (1.8 eV). For ease of viewing, raw data was transformed from %Reflectance R to Absorbance A according to A = log (1/R).[16]

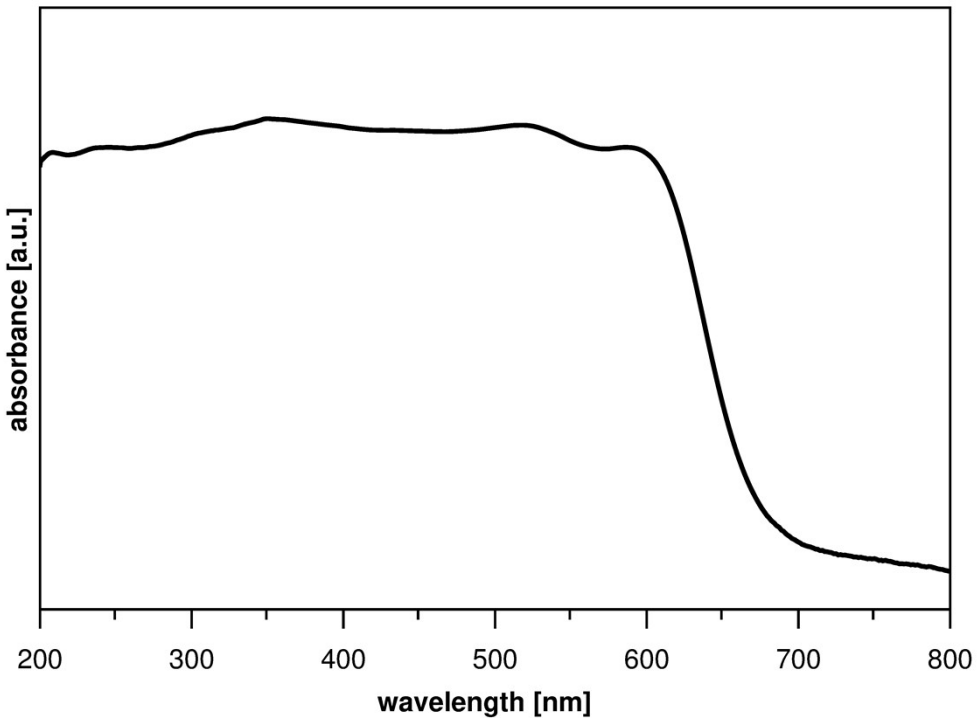

Figure S7. Optical absorption spectrum of **1**, measured in diffuse reflectance.

Details of Computational Studies

Density functional theory (DFT) calculations were performed with the Vienna Ab initio Simulation Package (VASP 5.4.4).[17-19] The projector-augmented wave (PAW) method was used in conjunction with the "standard" pseudo potentials for all atoms (version PBE5.4).[20] Dispersion interactions were captured with the DFT-D3 scheme using the Becke-Johnson-type damping function.[21],[22] The precision tag was set to "accurate", a total energy difference of at most 10^{-5} eV was used for SCF convergence while setting the plane wave energy cutoff to 400 eV. All calculations were done with a Γ-centered 1×2×1 k-mesh. The mesh containing twice as many k-points is more favorable in total energy by only 6 kJ/mol indicating very good convergence. For structure optimization, the generalized gradient approximation (GGA) based exchange-correlation functional proposed by Perdew, Burke and Ernzerhof (PBE)[23] was used without spin-orbit coupling (SOC).[24] The force convergence criterion was 10^{-2} eV/Å. Further electronic structure analysis calculations do include SOC except Crystal Orbital Hamilton Population (COHP). HSE06 and TB09 calculations were carried out on the optimized PBE structure. All convergence criteria were kept identical and SOC was included.

Periodic energy decomposition analysis (pEDA)[25] and QTAIM[26],[27] were calculated with the Amsterdam Modeling Suite (AMS-BAND 18.105)[28-31] while sampling k-space at the Γ-point. Again, the PBE-D3(BJ) functional was used in conjunction with the atom centered DZP[32-34] basis set and a 'large' frozen core. Numerical quality was set to 'Good'. Scalar relativistic effects were included.

Raw data is available at the NOMAD repository. DOI:
http://dx.doi.org/10.17172/NOMAD/2019.06.27-1

Atomic structure:

Table S5: Crystallographic data for **1** compared to calculation.

	Experiment	Theory	Δ%
a / Å	14.4647	14.2472	-1.5
b / Å	7.5084	7.4070	-1.4
c / Å	20.9965	20.8340	-0.8
α / °	90	90.015	0.0
β / °	108.165	108.603	0.4
γ / °	90	89.987	0.0
V / Å^3	2166.7	2083.7	-3.8
d(Bi-Bi) / Å	4.349	4.277	-1.7
d(I-I) / Å	3.839	3.692	-3.8

The structural optimization starting from the experimentally derived structure leads to good agreement with deviations of <1.5% in lattice vectors and a slightly too short (<3.8%) interlayer I-I distances resulting in an underestimation in cell volume (<4%, Table S5). Starting from this structure, the band gap was derived from the density of states (DOS) with different density functionals. As shown in Table S6, the GGA-type functional PBE gives surprisingly good agreement with the experimentally derived band gap ($\Delta\Delta E_{gap}$ <0.2 eV), although this functional class is known to often underestimate the gap due to the self-interaction error.[35]

Consequently, the HSE06 functional including Hartree-Fock type exchange – which usually corrects this underestimation – now gives a too large band gap. The best agreement to experiment is found for the TB09 functional, which contains one additional parameter fitted to semiconductor band gaps and has been found to perform very well for other materials in the past by us and others.[36],[37] This lends confidence to choosing the more computationally efficient PBE functional for further investigations of the electronic structure.

Table S6. Band gap (ΔE_{gap}) from density of states calculations including spin-orbit coupling effects with different density functionals.

Method	ΔE_{gap} in eV
Experiment (this study)	1.8
PBE [23]	1.64
HSE06 [39]	2.23
TB09 [36]	1.87

Table S7. Results from AIM bond critical point analysis for iodine-iodine contacts. The electron density is given in e*a0^{-3}.

	Interlayer I-I	Intralayer I-I
ρ	0.0128	0.0072
$\nabla^2\rho$	0.0281	0.0160

Table S8. Results of energy decomposition analysis for extended systems (pEDA) for 1. Fragments are outlined in Figure S8a.

ΔE_{int}	-598
ΔE_{int}(disp)[a]	-317 (53%)
ΔE_{int}(elec)[a]	-281 (47%)
ΔE_{Pauli}	509
ΔE_{elstat}[b]	-445 (56%)
ΔE_{orb}[b]	-344 (44%)
ΔE_{orb}(I-I)[c]	-146 (42%)

[a] Percentage values give the relative contributions of dispersion and electronic effects to ΔE_{int}; [b] percentage values give the relative contributions to the attractive pEDA terms ΔE_{elstat} and ΔE_{orb}; [c] percentage values give the relative contributions to ΔE_{orb} from the NOCV scheme. All energies are given in kJ mol^{-1}.

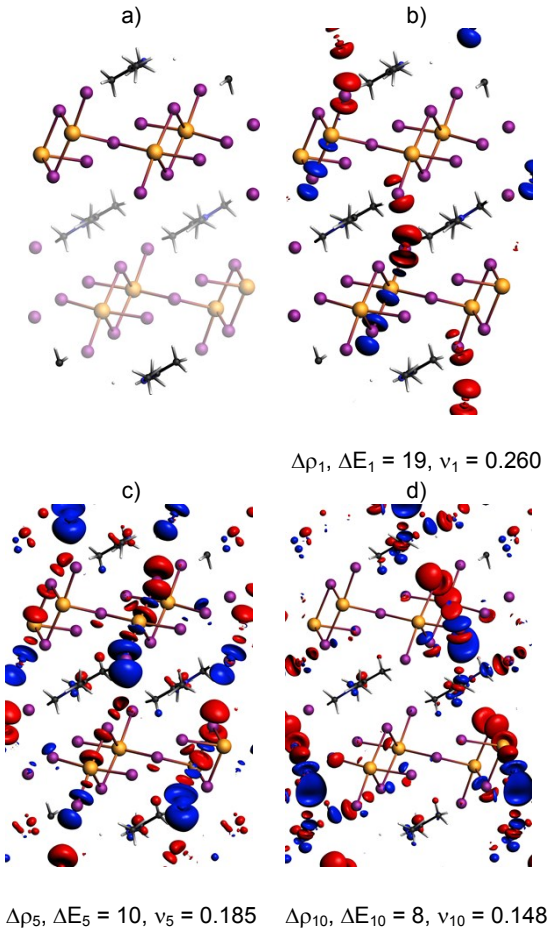

Figure S8. a) Fragments used for pEDA. b-d) deformation densities (Δρ) showing the charge accumulation (blue) and depletion (red) in the iodine layers. Every Δρ is fourfold degenerate (only one example shown) and slightly different isovalues have been used for visual clarity (b: $3*10^{-5}$, c: $5*10^{-6}$, d: $3*10^{-6}$).

We can identify 12 deformation densities that clearly show charge flow between non-bonding electron pairs of the iodine atoms, three of them are shown in Figure S8.The largest charge shift is seen here toward the edge-sharing iodine atoms ($\Delta\rho_{1\text{-}4}$; Fig. S8b) which contributes 74 kJ mol^{-1} (21%) to the orbital stabilization term and leads to slightly larger negative charge at these atoms (q(AIM) = -0.41 e; corner-sharing and terminal I-atoms q(AIM) = -0.37/-0.39 e).

The polarization of iodine atoms thus makes up 42% of the stabilizing orbital interactions and is the major contribution here. The remaining deformation densities are numerous and very small and do not allow further interpretation. But the total deformation density (as sum of all individual densities) is in very good agreement with the commonly used charge density difference and confirms that the iodine-iodine charge shift is the major contribution (Figure S9).

Comparison of charge density difference plot and deformation density from intermediate to final wavefunction in pEDA:

a) b)

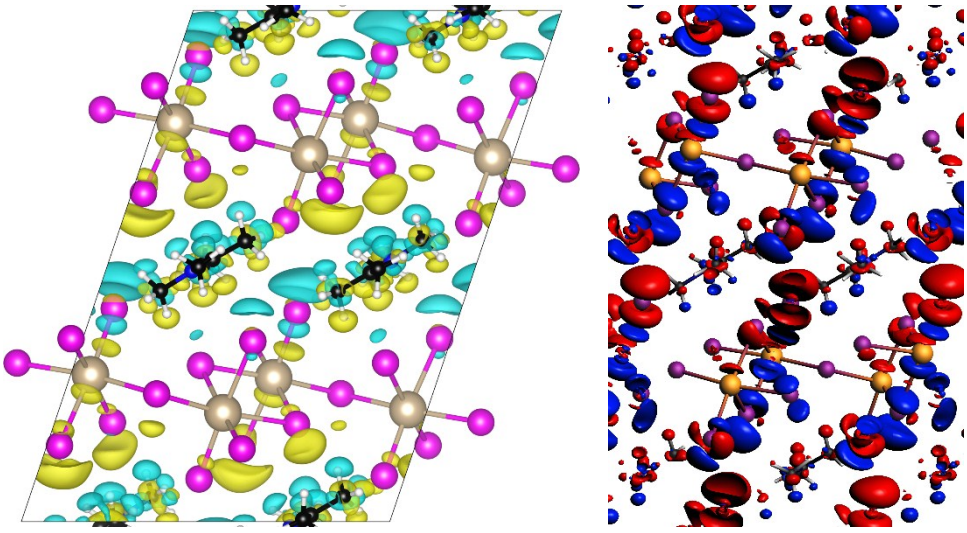

Figure S9: a) Charge density difference plot. Yellow: accumulation of charge density. Cyan: depletion of charge density. Electron density is mainly redistributed within the $[Bi_2I_7]^-$ layer due to its larger polarizability compared to the organic layer. b) Deformation density. Blue: accumulation of charge density. Red: depletion of charge density. The resulting picture is rather similar but the shape of the orbitals where density either flows to or from is more clearly visible. Also, the polarization of the organic layer is already considered so the deformation density is more concentrated in the relevant parts of the structure.

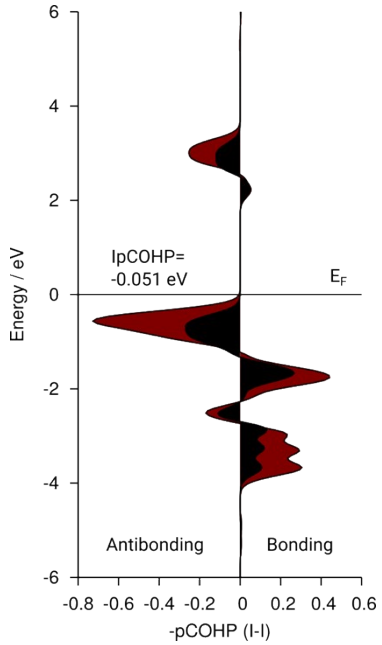

Figure S10. Negative of the pCOHP values of the interlayer I-I bond elongated by 9.6% (shaded black) in comparison to the pCOHP of the optimized structure (red areas).

References

[1] M. Ruck, *Z. Kristallogr.,* 1995, **210**, 650-655.

[2] T. Li, Y. Hu, C. A. Morrison, W. Wu, H. Han and N. Robertson, *Sustainable Energy Fuels,* 2017, **1**, 308-316.

[3] a) G. M. Sheldrick, *Acta Cryst.,* 2008, **A64**, 112-122; b) G. M. Sheldrick, *Acta Cryst.,* 2015, **A71**, 3-8; c) G. M. Sheldrick, *Acta Cryst.,* 2015, **C71**, 3-8.

[4] O. V. Dolomanov, L. J. Bourhis, R. J. Gildea, J. A. K. Howard and H. Puschmann, *J. Appl. Crystallogr.,* 2009, **42**, 339-341.

[5] K. Brandenburg, Diamond, Crystal Impact GbR: Bonn, Germany, 2005.

[6] L. M. Trefonas, R. L. Flurry Jr., R. Majeste, E. A. Meyers and R. F. Copeland, *J. Am. Chem. Soc.,* 1966, **88**, 2145-2149.

[7] O. Knop, T. S. Cameron, P. K. Bakshi, W. Kwiatkowski, S. C. Choi and D. Adhikesavalu, *Can. J. Chem.,* 1993, **71**, 1495-1523.

[8] M. Lindsjö, A. Fischer and L. Kloo, *Z. Anorg. Allg. Chem.,* 2005, **631**, 1497-1501.

[9] N. Louvain, N. Mercier and F. Boucher, *Inorg. Chem.,* 2009, **48**, 879-888.

[10] A. García-Fernández, I. Marcos-Cives, C. Platas-Iglesias, S. Castro-García, D. Vázquez-García, A. Fernández and M. Sánchez-Andújar, *Inorg. Chem.,* 2018, **57**, 7655−7664.

[11] H.-L. Sheu and J. Laane, *Inorg. Chem.,* 2013, **52**, 4244−4249.

[12] R. Kuhn and H. Schretzmann, *Chem. Ber.,* 1957, **90**, 557-564.

[13] N. J. Leonard and J. V. Paukstelis, *J. Org. Chem.,* 1963, **28**, 3021-3024.

[14] J. Laane and P. W. Jagodzinski, *Inorg. Chem.,* 1980, **19**, 44-49.

[15] S. Öz, J.-C. Hebig, E. Jung, T. Singh, A. Lepcha, S. Olthof, J. Flohre, Y. Gao, R. German, P. H. M. van Loosdrecht, K. Meerholz, T. Kirchartz and S. Mathur, *Sol. Energ. Mat. Sol. Cells,* 2016, **158**, 195-201.

[16] S. I. Boldish and W. B. White, *Am. Mineral.,* 1998, **83**, 865-871.

[17] G. Kresse and J. Hafner, *Phys. Rev. B,* 1993, **47**, 558.

[18] G. Kresse and J. Furthmüller, *Comput. Mater. Sci.,* 1996, **6**, 15-50.

[19] G. Kresse and J. Furthmüller, *Phys. Rev. B,* 1996, **54**, 11169.

[20] G. Kresse and D. Joubert, *Phys. Rev. B,* 1999, **59**, 1758.

[21] S. Grimme, J. Anthony, S. Ehrlich and H. Krieg, *J. Chem. Phys.,* 2010, **132**, 154104.

[22] S. Grimme, S. Ehrlich and L. Goerigk, *J. Comput. Chem.,* 2011, **32**, 1456-1465.

[23] J. P. Perdew, K. Burke and M. Ernzerhof, *Phys. Rev. Lett.,* 1996, **77**, 3865.

[24] S. Steiner, S. i Khmelevskyi, M. Marsmann and G. Kresse, *Phys. Rev. B,* 2016, **93**, 224425.

[25] M. Raupach and R. Tonner, *J. Chem. Phys.,* 2015, **142**, 194105.

[26] J. I. Rodriguez, A. M. Köster, P. W. Ayers, A. Santos-Valle, A. Vela, G. Merino, *J. Comput. Chem.,* 2009, **30**, 1082-1092.

[27] J. I. Rodriguez, R. F. W. Bader, P. W. Ayers, C. Michel, A. W. Gotz and C. Bo, *Chem. Phys. Lett.,* 2009, **472**, 149-152.

[28] a) G. te Velde and E. J. Baerends, *Phys. Rev. B,* 1991, **44**, 7888; b) G. Wiesenekker and E. J. Baerends, *J. Phys. Condens. Matter,* 1991, **3**, 6721.

[29] M. Franchini, P. H. T. Philipsen and L. Visscher, *J. Comput. Chem.,* 2013, ***34***, 1819-1827.

[30] M. Franchini, P.H.T. Philipsen, E. van Lenthe and L. Visscher, *J. Chem. Theory Comput.,* 2014, **10**, 1994-2004.

[31] BAND2018, SCM, Theoretical Chemistry, Vrije Universiteit, Amsterdam, The Netherlands, http://www.scm.com.

[32] E. van Lenthe and E. J. Baerends, *J. Comput. Chem.,* 2003, **24**, 1142-1156.

[33] D. P. Chong, E. van Lenthe, S. J. A. van Gisbergen and E. J. Baerends, *J. Comput. Chem.,* 2004, **25**, 1030-1036.

[34] D. P. Chong, *Mol. Phys.,* 2005, **103**, 749-761.

[35] J. P. Perdew, *Int. J. Quantum Chem.,* 1985, **28**, 497-523.

[36] F. Tran and P. Blaha, *Phys. Rev. Lett.,* 2009, **102**, 226401.

[37] P. Rosenow, L. C. Bannow, E. W. Fischer, W. Stolz, K. Volz, S. W. Koch and R. Tonner, *Phys. Rev. B,* 2018, **97**, 075201.

[38] A. V. Krukau, O. A. Vydrov, A. F. Izmaylov and G. E. Scuseria, *J. Chem. Phys*., 2006, **125**, 224106.